# Structural and Morphological Analysis of Poly(3-hexylthiophene ) at Surfaces and Interfaces

# Static and dynamic properties of poly(3-hexylthiophene) films at liquid/vacuum interfaces

Yeneneh Y. Yimer and Mesfin Tsige

## Additional information on J. Chem. Phys.
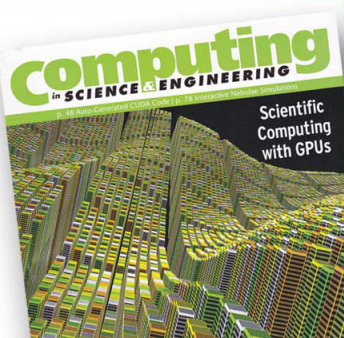
# Static and dynamic properties of poly(3-hexylthiophene) films at liquid/vacuum interfaces

Yeneneh Y. Yimer and Mesfin Tsige[a)]
*Department of Polymer Science, The University of Akron, Akron, Ohio 44325-3909, USA*

All-atom molecular dynamics simulations are used to study static and dynamic properties of poly(3-hexylthiophene) (P3HT) films at liquid/vacuum interfaces with regards to their dependence on both temperature and molecular weight. The static properties of the films are characterized by calculating specific volume, interfacial width, orientational ordering of the hexyl groups, and surface tension. The specific volume found to be a monotonically decreasing function of the molecular weight while its dependence on temperature follows the Simha-Somcynsky's equation of state. The orientational ordering calculations show the hexyl groups protruding from the vacuum side of the interface, where the degree of order at the interface is found to be strongly dependent on both temperature and molecular weight. The surface tension values show a linear dependence on temperature and the molecular weight dependence is equally described by both $M^{-2/3}$ and $M^{-1}$ power law models. The dynamic properties are quantified by calculating diffusion coefficients for the chain centers-of-mass and thiophene ring segments as well as first-order and second-order end-to-end vector autocorrelations and chain backbone torsion autocorrelation. All calculated dynamic properties show strong dependence on both temperature and molecular weight. All the autocorrelations are well described by Kohlrausch-Williams-Watts equation. Our detailed analysis of the static and dynamic properties of P3HT films show that the calculated static and dynamic properties data can be fit with well-known polymer models. © *2012 American Institute of Physics*. [http://dx.doi.org/10.1063/1.4767395]

## I. INTRODUCTION

Solar energy is one of the most abundant and renewable energy sources. Progress has been made to utilize this energy, especially in making solar cell devices, however, the economic feasibility of solar cell devices has been limited by the high cost of materials and fabrication. Of those devices, polymer-based photovoltaics are promising because their easy and inexpensive processing techniques, their compatibility with flexible substrates, their being semi-transparency and their being light-weight, and possibility of chemically tuning their properties. However, the power conversion efficiency of polymer-based solar cells is still low compared to their inorganic counterparts.

Poly(3-hexylthiophene) (P3HT) is one semiconducting polymer commonly used in organic photovoltaic (OPV) devices, due to its high electrical conductivity, good thermal stability and solution processibility.[1–3] One of the most widely studied and promising donor-acceptor bulk heterojunction (BHJ) systems is based on P3HT and fullerene derivatives such as [6,6]-phenyl-C61-butyric acid methyl ester (PCBM). The best reported power conversion efficiencies of P3HT:PCBM-based BHJ solar cell has reached to 6.5%.[4,5] For OPVs to be commercially viable, the efficiency should be higher than 10%,[6] with lifetime greater than 3–4 years.[7] In BHJ devices, blends of donor and acceptor molecules ideally should undergo nanoscale phase separation for charge generation at the interfaces, and form bicontinuous percolating pathways for efficient charge transport to the electrodes. However,

the nanoscale morphology of the BHJ depends on several factors, such as ratio of donor to acceptor, molecular weight, type of solvent, processing temperature, solution concentration, thermal annealing, etc. The full extent of these factors on the device morphology is still not well understood. Thus, to improve the performance of P3HT-based devices, understanding the structural packing, morphology, and chain dynamics of P3HT, both in the bulk and at the interfaces is important.

Recent experimental studies of P3HT:PCBM BHJ films suggest that amorphous PCBM is dispersed in amorphous P3HT domains and remains segregated from the crystalline P3HT domains.[8,9] Three-dimensional morphological study of P3HT:PCBM BHJ film using electron tomography revealed that the overall crystallinity of P3HT is as high as 60%,[10] which implies that the content of the amorphous domains is significant. Most previous studies have given emphasis to the crystallinity of P3HT and the device, without explicitly addressing the effects of the amorphous domains of P3HT on device performance. In a very recent experimental study, Vakhshouri *et al.*,[11] examined the electron mobility in amorphous P3HT and PCBM blends and found that miscibility of the components strongly affects electron transport within blends. To improve device performance, understanding the amorphous domains of P3HT is as important as understanding the crystalline domains.

Thermal annealing of P3HT films is usually done below the bulk melting temperature. However, annealing of P3HT on a hydrophobized substrate above its bulk melting temperature resulted in pronounced ordering of P3HT chains.[12] Heating poly(3-alkylthiophene) (P3AT) films above their melting

---

a)Electronic mail: mtsige@uakron.edu.

temperatures and then recrystallizing just below their melting temperatures resulted in maximum order of P3AT.[13] It is probably reasonable to assume that the amorphous regions of a P3HT semi-crystalline film may have similar structure to the melt if the film is prepared by annealing it above its melting temperature. It is also very likely that the specific surface groups that are present in the melt state would also be preferred in the crystal state below the bulk melting temperature. Thus, investigating the behavior of P3HT in its melt state can provide more insight into the morphological and structural properties of P3HT in the amorphous phase and the surface properties of the crystalline phase.

The morphological and structural characterizations of P3HT and its blends are mostly done using several techniques such as: transmission electron microscopy, atomic force microscopy, electron tomography, X-ray diffraction, near edge x-ray absorption fine structure, etc. Experimental evidences for the molecular-scale structure and morphology of P3HT and its blends remain a challenge in varying degrees. Simulations, in combination with the experimental methods, can be used to advance the understanding at molecular level. Molecular dynamics (MD) is a powerful computational technique that can be used to understand the morphological evolution both in bulk and at interfaces. It is also capable of predicting material properties in different experimental conditions with atomistic detail. The accuracy of MD depends on the ability of the force field to correctly capture the interactions between atoms in the system.

Using molecular dynamics simulation in our recent work,[14] we investigated the structural and interfacial properties of free-standing melt P3HT films for one molecular weight at different temperatures. However, the molecular weight dependence of those properties was not investigated. Experimental studies have shown that the morphology of P3HT and device performance based on P3HT are strongly dependent on molecular weight.[15–17] In addition, the surface tension which plays an important role in determining interfacial properties of the P3HT film such as wetting, coating blending, and adhesion is expected to show strong dependence on molecular weight. To the best of our knowledge, there has been no experimental or computational study in the literature that specifically addresses the molecular weight dependence of the surface tension of P3HT films. Hence, in this study, in addition to thoroughly investigating other important surface properties, we have also investigated the molecular weight dependence of the surface tension of P3HT films at liquid/vacuum interfaces.

It is also very important to note that the performance of the devices is strongly dependent on the thermodynamic stability of the resulting morphology, which is directly related to the dynamics and relaxation of the P3HT chains. Therefore, in order to have a full understanding of the formation and stability of the morphology, one also has to quantify the dynamic properties of the P3HT film in addition to its static properties.

The main objective of the present study is, therefore, to investigate the static and dynamic properties of free-standing P3HT films using all-atom molecular dynamics simulations. More specifically, we assess the dependencies of those properties on both molecular weight and temperature. To charac-

terize the static properties of the films, we computed mass density, interfacial width, side-chain orientation, and surface tension of the films at liquid/vacuum interfaces. As part of an investigation of the dynamic properties of the P3HT films, the following dynamic parameters were evaluated: chain center-of-mass and thiophene ring segment diffusion coefficients, the first-order and second-order end-to-end vector autocorrelation and backbone chain torsion autocorrelation. In Sec. II, we will discuss the details of our simulation procedures. The results and discussion are presented in Sec. III followed by the summary and conclusions.

## II. SIMULATION DETAILS

In this work, all-atom molecular dynamics simulations have been employed to study static and dynamic properties of free-standing melt P3HT films. The details of the force field parameters used in the present study have been discussed in detail in our previous paper.[14] Briefly, the force field was proposed by Huang *et al.*[18] and validated for melt P3HT by the same group.[18–20] The force field parameters for the chain backbone (partial charges, bonds and angles) were based on model tetrathiophene,[21] and the dihedral torsion potential was based on the results of *ab initio* calculations of 3HT oligomers.[22] The van der Waals interactions are described by the Lennard-Jones 12-6 potential, and the parameters $\sigma_{ij}$ and $\epsilon_{ij}$ were obtained from the OPLS-AA force field.[23] For the hexyl groups, all force field parameters were taken from the OPLS-AA force field for *n*-alkanes.[23]

In this study, we consider 100% regioregular P3HT chains of four different chain lengths: 10, 20, 30, and 40 monomer units. Simulation systems comprised 100, 76, 68, and 72 P3HT chains, with 25200, 38152, 48128, and 72144 total atoms, respectively. The initial configurations of the systems were generated by randomly placing the chains in rectangular periodic simulation boxes at a density of 0.9 g/cm³. The length of the box along the z-axis was chosen such that a fully stretched chain cannot participate at both interfaces at the same time. That is why the total number of atoms in the simulation cell increased with chain length in our simulation and the film thickness varies with chain length (as can be seen in Figure 4).

The initial equilibrations of the systems were carried out in two steps—first, the systems were run in the NPT ensemble at a temperature of 600 K, far above the melting temperature of P3HT[12, 24–28] and at a pressure of 1 atm for 5 ns, which allowed the systems to adjust to their melt densities at this temperature. The systems were further equilibrated in the NVT ensemble for 5 ns at the same temperature. Once equilibrium in the NVT ensemble had been established, films with surfaces in the *xy*-plane were created by removing the periodicity along the *z*-direction. To ensure that periodic images of the resulting films did not interact in the *z*-direction, the simulation box length in the *z*-direction was significantly increased. The films were then run in the NVT ensemble at temperatures ranging from 540 K to 660 K in increments of 20 K, well above the melting temperature of P3HT.[12, 24–28]

All simulations were carried out using the LAMMPS simulation package.[29] The equations of motion were integrated

using the velocity-Verlet algorithm using a time step of 1 fs. For both NPT and NVT ensembles, a Nosé-Hoover thermostat with a damping time of 100 fs was used to maintain the temperature of the system. For the NPT ensemble, an additional Nosé-Hoover barostat with a 1 ps damping time was used to keep the pressure of the system at 1 atm. For the non-bonded interactions, the cutoff radius was fixed at 12 Å, and the long-range Coulomb interactions (beyond the cutoff radius) were calculated using the particle-particle/particle-mesh Ewald algorithm.[30] The surface tension calculations required that the systems be equilibrated for a long time from –70 to 260 ns, depending on the temperature and chain length.

To circumvent the very long surface equilibration time, attempts were made to use a united-atom (UA) force field for the hexyl side chains, keeping the all-atom force field for the chain backbone. The UA force field we used in the present study was first reported by Escobado et al.,[31] and recently Amat et al.,[32] used it to study interfacial properties of n-alkanes and perfluoroalkanes. For n-alkanes using this UA model, the obtained surface tension values were 9.2% to 23.7% higher than reported experimental values and also all-atomic simulations.[32] Using this UA model, we were able to reduce the surface equilibration times by a factor of 1/2. However, we obtained surface tension values which are 14% to 25% lower than our all-atom simulations results. Though all-atom simulation is computationally very expensive, the large discrepancy between the results generated using united atom and all-atom simulation necessitated the use of all-atom simulations in the present study.

## III. RESULTS AND DISCUSSION

### A. Static properties

To characterize the physical properties of the films, quantifying both their static and dynamic properties is important. The main focus of this section is to provide detailed analysis of the static properties of the films. Based on their origins, static properties can be categorized as structural or thermodynamic. Structural quantities have been described by calculating the mass density profiles and interfacial widths of the films. Moreover, the chain orientations in different parts of the film have been investigated. Of thermodynamic quantities, the surface tension values of the films at the liquid/vacuum interfaces have been calculated.

#### 1. Mass density

The mass density profile, $\rho(z)$, of each film was calculated by partitioning the simulation cells into bins along the z-direction, with bin thickness $\Delta z = 1$ Å, and summing the masses of atoms in each bin, and divided by partition volume. Figure 1 shows representative mass density profiles, averaged over the last 2 ns of each simulation, for systems made of 40-mers chains at three different temperatures (540 K, 600 K, and 660 K).

At liquid/vacuum interfaces, the mass density decays smoothly to zero, exhibiting the characteristic sigmoidal shape typical of free liquid surfaces.[33,34] As the temperature
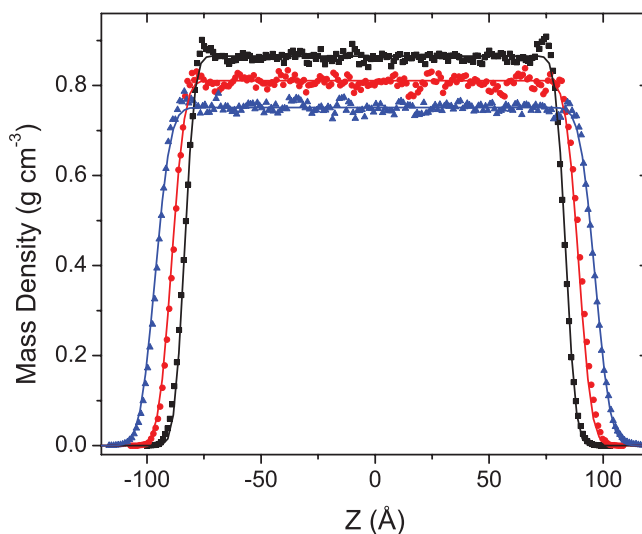


FIG. 1. Average mass density profiles of films made of 40-mers chains at 540 K (squares), 600 K (circles), and 660 K (triangles). $Z = 0$ is the center of the film and the solid lines are the fits to the density profiles using Eq. (1).

decreases from 660 K to 540 K, the liquid/vacuum interfaces become sharper. To better characterize the interfaces, the interfacial widths of the films were obtained by fitting the mass density profiles to an error function,[35,36]

$$\rho(z) = \frac{\rho_l - \rho_v}{2}\left(erf\left(\frac{(|z_0| - |z|)}{\sqrt{2}\triangle}\right) + 1\right), \qquad (1)$$

where $\rho_l$ and $\rho_v$ are the averaged densities of the liquid and the vacuum phases, respectively, $\triangle$ is the interfacial width and $z_0$ is the position of the Gibbs dividing surface. As depicted in Figure 1 by the solid lines, Eq. (1) fits the density profiles very well, especially at the interfaces. For different chain lengths, the obtained interfacial widths have been plotted in Figure 2 as functions of temperature. As can be seen in the figure in general, interfacial width increases with increasing temperature. At high temperatures (>600 K), the interfacial widths
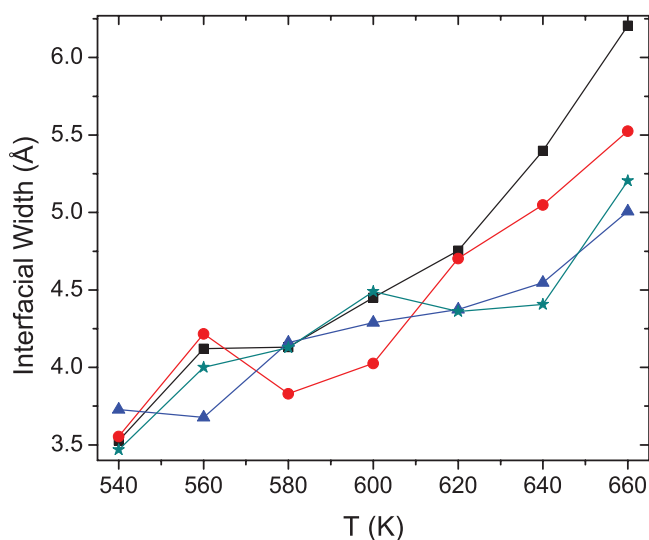


FIG. 2. Interfacial width as a function of temperature for P3HT systems comprising chains of length 10 (squares), 20 (circles), 30 (triangles), and 40 (stars). The solid lines are included as a guide to the eye.
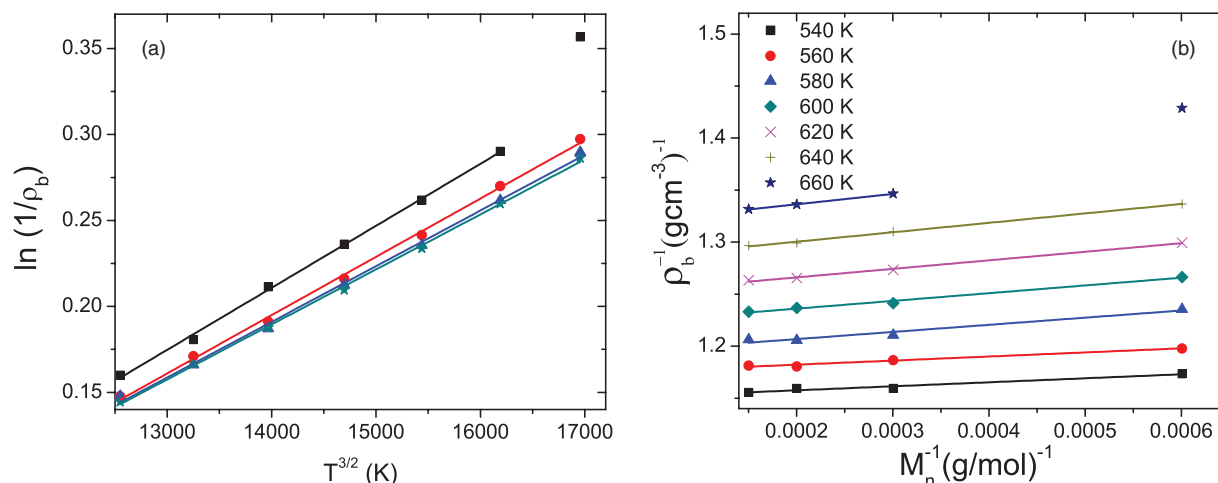
FIG. 3. (a) Temperature dependence of specific volume for P3HT systems comprising chains of length 10 (squares), 20 (circles), 30 (triangles), and 40 (stars) monomers. The solid lines are fit to the data using Eq. (2). (b) The molecular weight dependence of specific volume at seven different temperatures (540 K to 660 K in steps of 20 K). The solid lines are fit to the data using Eq. (3).

decrease as the chain lengths increase. However, at low temperatures there is no clear chain length dependence.

In the middle region of the film, the mass density (see Figure 1) is fairly constant. By taking the time average of the mass density in this region, the bulk density, $\rho_b$, can be calculated. The dependence of the calculated bulk density on temperature and chain length are shown in Figures 3(a) and 3(b), respectively. As can be seen in the figures, the bulk density of the 10-mers chains at 660 K shows deviation from the observed trends for the other temperatures. To understand the cause of this deviation, we looked at the time evolution of the film. We observed that after very long simulations (>50 ns), only a few chains had left the film surface, which would imply that the film had started to degrade. In all-atom simulations of polymer films containing bulky molecules like P3HT, observing degradation in a reasonable computational time is not easy. For this particular film we are able to observe the film degradation within our simulation time scale. In a recent experimental study utilizing thermogravimetric analysis, P3HT films in air were seen to undergo thermal degradation at 693 K.[37] For short chains or low molecular weights, the degradation temperature is lower. For this reason bulk density of the 10-mers chains at 660 K will not be considered in the following bulk density analysis.

For polymers in the melt state at zero pressure, the specific volume, $\frac{1}{\rho_b}$, and temperature[38] are expected to follow the Simha-Somcynsky equation of state,[39] given by

$$ln\left(\frac{1}{\rho_b}\right) = b_1 + b_2 T^{3/2}, \tag{2}$$

where $b_1$ and $b_2$ are constants. Figure 3(a) shows the temperature dependence of specific volume and the corresponding fits to the data using Eq. (2). The parameters obtained from the fitting are tabulated in Table I. As shown in the table, the linear correlation coefficient values are $R^2 \approx 0.998$, implying excellent fits to the bulk density data. Moreover, the obtained values of $b_1$ and $b_2$ are in good agreement with previous reported values for different polymers in the melt state.[38]

For homologous series, the bulk properties vary linearly with the reciprocal of the molecular weight;[40–45] the specific volume is one such property. The molecular weight dependence of the specific volume is given by

$$\frac{1}{\rho_b} = \frac{1}{\rho_\infty} - \frac{k_b}{M_n}, \tag{3}$$

where $\rho_\infty$ is bulk density at infinite molecular weight, $M_n$ is number-average molecular weight, and $k_b$ is a constant. This relation suggests that, at constant temperature and pressure, the free-volume contribution from the end groups of a polymer chain is independent of $M_n$.

Figure 3(b) shows the dependence of the specific volume on the molecular weight. The specific volume increases linearly with decreasing molecular weight. Equation (3) fits the specific volume data very well as shown by solid lines in the figure and the parameters obtained from the fits are tabulated in Table II. The dependence of the bulk density on molecular weight is attributed to the change in the concentration of chain end groups with molecular weight.[46,47]

### 2. Chain orientation

For free-standing films made of 10-mers chains, the orientations of different parts of the chains were investigated in detail in our recent work.[14] Lacking from that study was the chain-length dependence of the orientations of different parts of the chains. The hexyl groups dominate at the interface, hence we focus on the dependence of the hexyl-group

TABLE I. Parameters extracted from fitting the bulk density using Eq. (2) where $R^2$ is the linear correlation coefficient.

| Chain length | $b_1$ (cm$^3$g$^{-1}$) | $b_2$ ($\times 10^{-5}$ cm$^3$g$^{-1}$K$^{-3/2}$) | $R^2$ |
|---|---|---|---|
| 10 | −0.2942(96) | 3.6069(668) | 0.998 |
| 20 | −0.2798(93) | 3.3907(632) | 0.998 |
| 30 | −0.2624(105) | 3.3907(711) | 0.998 |
| 40 | −0.2585(72) | 3.1998(485) | 0.998 |

TABLE II. Parameters extracted from fitting the specific volume data using Eq. (3) where $R^2$ is linear correlation coefficient.

| $T$ (K) | $\frac{1}{\rho_{b\infty}}$ (g cm$^{-3}$)$^{-1}$ | $k_b$ (mol$^{-1}$ cm$^3$) | $R^2$ |
|---|---|---|---|
| 540 | 1.1499(20) | 38.53(564) | 0.938 |
| 560 | 1.1744(15) | 39.27(418) | 0.967 |
| 580 | 1.1930(32) | 68.72(897) | 0.950 |
| 600 | 1.2212(18) | 74.36(498) | 0.987 |
| 620 | 1.2497(13) | 82.06(369) | 0.994 |
| 640 | 1.2823(11) | 90.63(303) | 0.997 |
| 660 | 1.3164(7) | 99.70(328) | 0.998 |

TABLE III. Total surface tension values of P3HT systems of different chain lengths at different temperatures. The unit of surface tension is mN m$^{-1}$.

| $T$ (K) | Chain length | | | |
|---|---|---|---|---|
| | 10 | 20 | 30 | 40 |
| 540 | 17.27 | 20.17 | 21.12 | 22.01 |
| 560 | 15.87 | 18.39 | 20.28 | 20.67 |
| 580 | 14.64 | 17.37 | 19.35 | 19.78 |
| 600 | 12.90 | 16.08 | 17.58 | 18.35 |
| 620 | 11.47 | 15.18 | 16.42 | 17.60 |
| 640 | 10.58 | 13.29 | 15.23 | 15.96 |
| 660 | 9.03 | 12.43 | 14.09 | 15.30 |

orientation on the chain-length. An orientational order parameter can be calculated using the second-order Legendre polynomial, which is given by

$$P_2(z) = \frac{1}{2}\langle 3\cos^2(\theta) - 1 \rangle, \tag{4}$$

where $\theta$ is the angle between the $z$-axis, i.e., the normal to the interface, and the orientational vector of the hexyl group, which is defined by the vector originating from the carbon atom on the thiophene ring to which the hexyl group is attached and ending on the carbon atom of the methyl group. The average, denoted by angle brackets, was taken over all possible orientations and time steps within a specified slice of width $\Delta z = 3.0$ Å over a given region in the $z$-direction.

The average orientational order parameter, $P_2(z)$, of the hexyl groups for four different chain lengths at 540 K and 620 K is shown in Figure 4. In the middle part of the films, $P_2(z) \approx 0$, implying that the orientations are essentially random. At the interface (or close to the surface), $P_2(z) > 0$, suggesting that the hexyl groups preferentially orient parallel to the surface normal, and the orientational ordering increases with decreasing temperature. Moreover, at the interface, the ordering of the hexyl groups increases with increasing chain length. This has consequences for the chain-length dependence of the surface tension at a given temperature, which is presented below.

### 3. Surface tension

For different films, surface tension values, $\gamma_p$, were calculated using the Kirkwood-Buff equation[48]

$$\gamma_p = \frac{L_z}{2}\left[\langle p_z \rangle - \frac{\langle p_x \rangle + \langle p_y \rangle}{2}\right], \tag{5}$$

where $\langle p_z \rangle$ and $\frac{\langle p_x \rangle + \langle p_y \rangle}{2}$ are normal and tangential pressure components, respectively. The angle brackets denote time averages, and the factor of 1/2 exists to account for the symmetry in the simulation box. To obtain convergent surface tension values, the simulations were run for 70 ns–260 ns, depending on chain length and temperature. The equilibration time increased with increasing chain length and decreasing temperature. We ran the simulations until the time variation of the surface tension did not seem to change any more and calculated the average over the last 10 ns of the simulations.

The surface tension calculated using Eq. (5) does not take into account the contribution of the Lennard-Jones interaction beyond the cut-off radius. The "tail correction," $\gamma_{tail}$, to the surface tension was calculated following the same procedure used in our previous work.[14] The overall surface tension of the system is given as the sum of the surface tension of the simulation result and the tail correction: $\gamma = \gamma_p + \gamma_{tail}$. In the remaining discussion, we use "surface tension" to refer
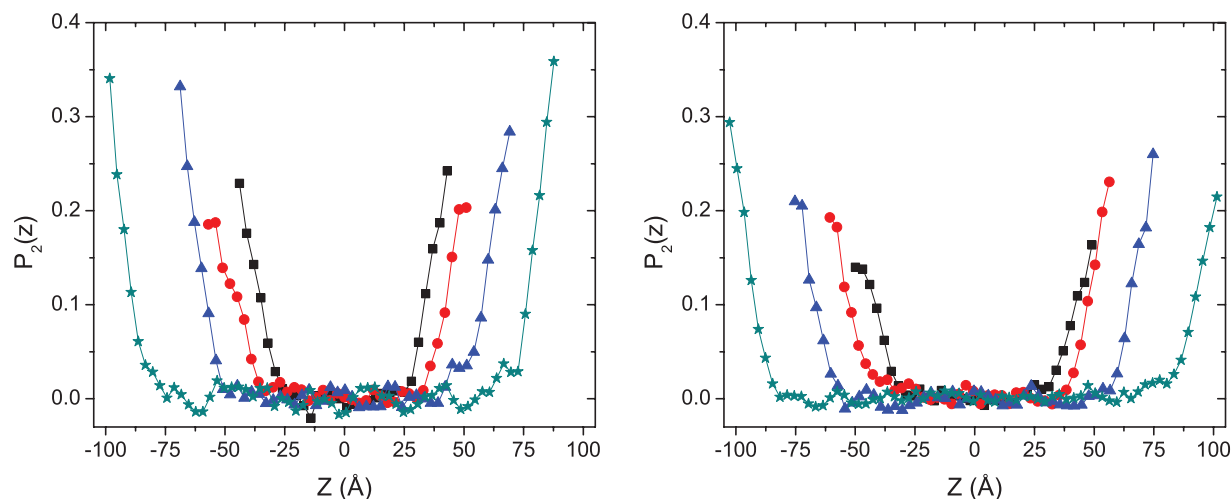


FIG. 4. Orientational order parameter profile, $P_2(z)$, of the hexyl groups of P3HT at 540 K (left) and 620 K (right) for systems comprising chains of length 10 (squares), 20 (circles), 30 (triangles), and 40 (stars) monomers. $Z = 0$ is the center of the film and the solid lines are guides to the eye.
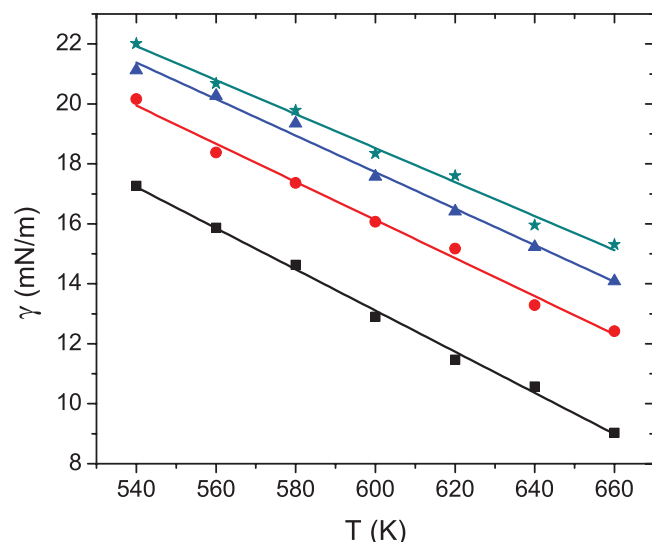
FIG. 5. Surface tension as a function of temperature for systems comprising chains of length 10 (squares), 20 (circles), 30 (triangles), and 40 (stars) monomers, and the solid lines are fits to the surface tension data using Eq. (6).

TABLE IV. Parameters extracted from fitting the surface tension data using Eq. (6) where $R^2$ is linear correlation coefficient.

| $M_n$ (kg mol$^{-1}$) | a (mN m$^{-1}$) | b (mN m$^{-1}$ K$^{-1}$) | $R^2$ |
|---|---|---|---|
| 1.66488 | 54.31(109) | 0.069(2) | 0.996 |
| 3.32775 | 54.28(147) | 0.064(3) | 0.992 |
| 4.99061 | 54.28(134) | 0.061(2) | 0.992 |
| 6.65348 | 52.55(122) | 0.057(2) | 0.992 |

The temperature dependence of surface tension can be described by the following linear relation:

$$\gamma = a - b * T, \tag{6}$$

where $b$ is the temperature coefficient and $a$ is a constant. Fits to the surface tension data using Eq. (6) are shown by the solid lines in Figure 5. The parameters obtained from the fits as well as the linear correlation coefficient, $R^2$, have been tabulated in Table IV. For all chain lengths, $R^2 > 0.99$ indicates Eq. (6) fits to the data very well.

The temperature coefficient, $b$, obtained from the fits decreases monotonically with increasing chain length. As the chain length increases, the chain conformations become more restricted and the surface entropy decreases, therefore the temperature coefficient, $b = \frac{d\gamma}{dT}$, is directly related to the surface entropy, which decreases with increasing chain length, consistent with our results. In previous experimental studies for liquid *n*-alkanes[52,53] and polystyrene,[54] similar chain length (molecular weight) dependence for this temperature coefficients was observed. Moreover, the obtained temperature coefficients are typical for other polymers,[55] including those with similar side chains.[56]

For homologous series, as the molecular weight increases, surface entropy decreases and surface tension increases. At infinite molecular weight, however, both surface entropy and surface tension converge to finite values. At

to "total surface tension" ($\gamma = \gamma_p + \gamma_{tail}$) unless otherwise mentioned.

The surface tension values for each system at different temperatures are tabulated in Table III. The calculated surface tension values are low, mainly due to the dominance of the hydrophobic hexyl side chains at interfaces.[14] To the best of our knowledge, there are no theoretical (excluding our recent work[14]) or experimental surface tension values available for melt P3HT in the literature. However, for solid-state P3HT, experimental reported values are in the range of 21–36 mN m$^{-1}$.[49–51] The surface tension of films in solid state is expected to be higher than in the liquid phase.

Figure 5 illustrates the temperature dependence of the surface tension. The surface tension, as can be seen in the figure, decreases monotonically with increasing temperature.
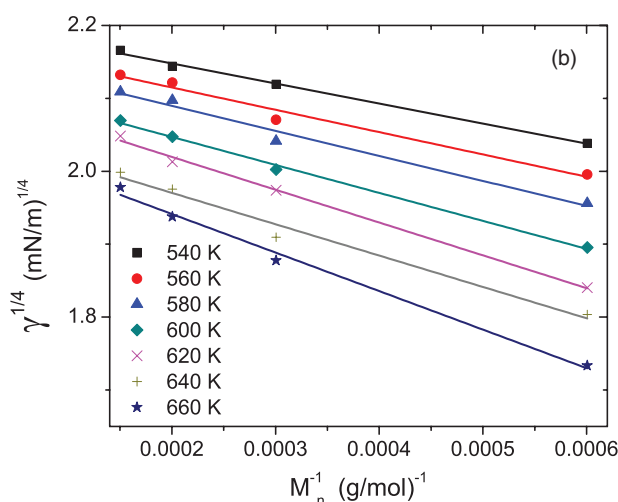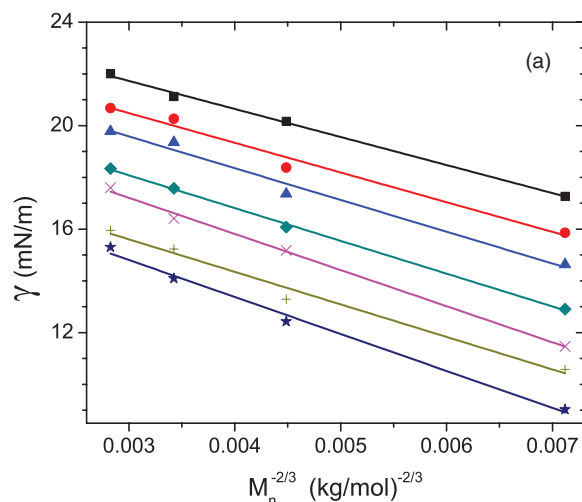


FIG. 6. Molecular weight dependence of surface tension (a) $\gamma$ vs. $M_n^{-2/3}$ (solid lines are fit to the data using Eq. (7)) and (b) $\gamma^{1/4}$ vs. $M_n^{-1}$ (solid lines are fit to the data using Eq. (8)) at seven different temperatures (540 K to 660 K in steps of 20 K).

TABLE V. Parameter values obtained from fitting surface tension data using Eqs. (7) and (8).

| T (K) | $\gamma_{\infty,1}(mNm^{-1})$ | $k_1(mNm^{-1}g^{-1}mol)$ | $R^2$ | $\gamma_{\infty,2}(mNm^{-1})$ | $k_2(mNm^{-1}g^{-1}mol)^{1/4}$ | $R^2$ |
|---|---|---|---|---|---|---|
| 540 | 24.98(18) | 1083.65(3863) | 0.996 | 23.56(5) | 275.44(1226) | 0.994 |
| 560 | 23.93(51) | 1147.89(10544) | 0.975 | 22.43(12) | 306.13(3187) | 0.968 |
| 580 | 23.27(51) | 1127.44(10739) | 0.977 | 21.70(12) | 343.12(3328) | 0.972 |
| 600 | 21.88(14) | 1267.16(2910) | 0.998 | 20.34(5) | 383.62(1479) | 0.996 |
| 620 | 21.40(26) | 1396.32(5446) | 0.995 | 19.81(6) | 449.83(1842) | 0.995 |
| 640 | 19.38(52) | 1257.38(11023) | 0.977 | 17.88(13) | 429.90(4139) | 0.973 |
| 660 | 19.10(40) | 1429.70(8360) | 0.990 | 17.56(10) | 528.39(3184) | 0.989 |

constant temperature and pressure, the molecular weight dependence of surface tension of polymer can be described by two distinct semi-empirical equations,[57]

$$\gamma = \gamma_{\infty,1} - k_1 M_n^{-2/3}, \qquad (7)$$

$$\gamma^{1/4} = \gamma_{\infty,2}^{1/4} - k_2 M_n^{-1}, \qquad (8)$$

where $\gamma_{\infty,1}$ and $\gamma_{\infty,2}$ are the surface tensions at infinite molecular weight and $k_1$ and $k_2$ are constants. Based on theoretical predictions,[58] Eqs. (7) and (8) are appropriate for low and high molecular weights, respectively. In spite of this, the difference in the surface tension values at infinite molecular weight, $\gamma_{\infty,1} - \gamma_{\infty,2}$, is in general less than 2 mN m$^{-1}$.[57]

Figure 6 depicts the molecular weight dependence of the surface tension. Fits to the surface tension data using Eqs. (7) and (8) are shown by the solid lines in Figures 6(a) and 6(b), respectively. The parameters obtained from the fit are tabulated in Table V. From the linear correlation coefficients, given in the table, we can conclude that the surface tension data fit both equations very well. The obtained values of $\gamma_{\infty,1} - \gamma_{\infty,2}$ are in the range of 1.42–1.59 mN m$^{-1}$, which is in good agreement with previous reported values for different polymers.[57]

The temperature dependence of $\gamma_{\infty,1}$ and $\gamma_{\infty,2}$ are shown in Figure 7. Both $\gamma_{\infty,1}$ and $\gamma_{\infty,2}$ decrease linearly with increasing temperature. The molecular weight of P3HT used in most experiments is usually larger than the ones used here. Hence, in an attempt to compare the simulation surface tension values with experiment, $\gamma_{\infty,1}$ and $\gamma_{\infty,2}$ were fit using Eq. (6) to illustrate their temperature dependance. From these fits for $\gamma_{\infty,1}$ and $\gamma_{\infty,2}$, the intercepts $a$ are 52.65 $\pm$ 2.02 mN m$^{-1}$ and 51.53 $\pm$ 1.83 mN m$^{-1}$, respectively, and temperature coefficients $b$ are 0.0511 $\pm$ 0.0034 mN m$^{-1}$ K$^{-1}$ and 0.0518 $\pm$ 0.0030 mN m$^{-1}$ K$^{-1}$, respectively. The obtained temperature coefficients are in the lower bound for polymers.[57] The temperature coefficients of polymers above and below the crystallization temperature are different,[56] thus we should not extrapolate the fit below the bulk crystallization temperature of P3HT, which is around 400 K.[59] However, the surface morphology of P3HT films is mainly dominated by hexyl groups, which crystallize at 333 K,[60] well below the P3HT melting temperature. To make a rough estimation of the surface tension at infinite molecular weight, we extrapolated $\gamma_{\infty,1}$ and $\gamma_{\infty,2}$ to room temperature and found values of 37.3 mN m$^{-1}$ and 36.0 mN m$^{-1}$, respectively, with the variation of the two surface tension values within the error margin. Based on the above hypothesis, we predict that at room temperature, the upper-end surface tension of P3HT at room
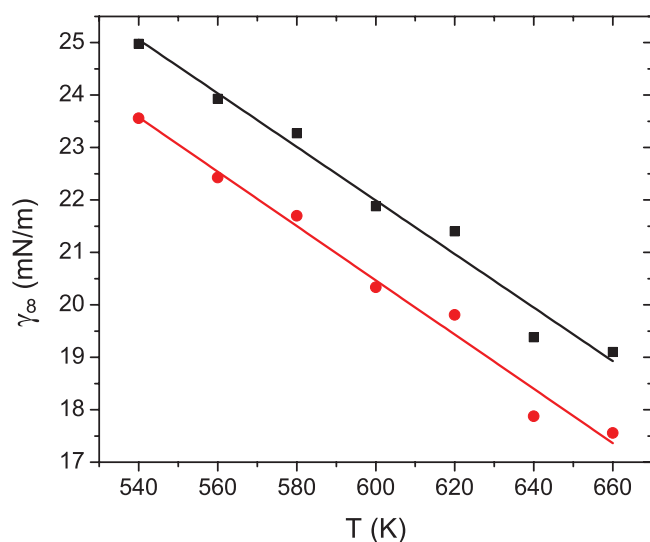


FIG. 7. Temperature dependence of surface tension at infinite molecular weight, $\gamma_{\infty,1}$ (squares) and $\gamma_{\infty,2}$ (circles). The solid lines are fits to surface tension values at infinite molecular weight using Eq. (6).
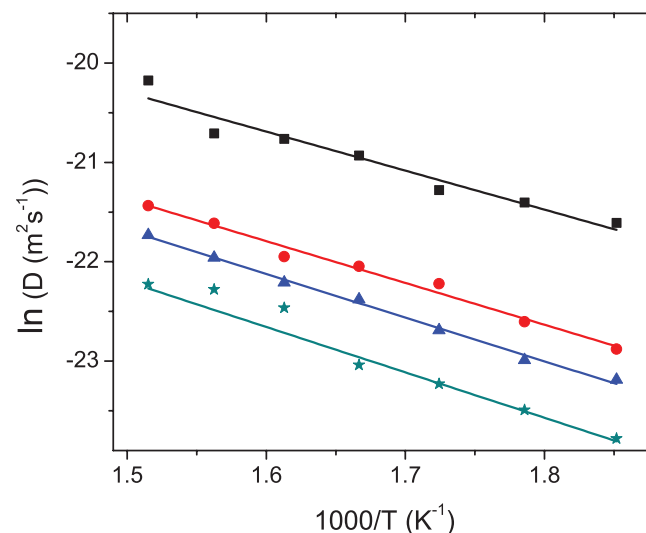


FIG. 8. Chain center-of-mass diffusion coefficient as a function of temperature for systems comprising chains of length 10 (squares), 20 (circles), 30 (triangles), and 40 (stars) monomers. The solid lines are fit to the data using Eq. (11).

TABLE VI. Values of parameters obtained from fitting the diffusion coefficient data using Eq. (11). The units of $D_0$ and $E_a^D$ are $10^{-7} \mathrm{m}^2\mathrm{s}^{-1}$ and kcal mol$^{-1}$, respectively.

| | | | | Thiophene ring center-of-mass | | | | | |
| | Chain center-of-mass | | | Bulk | | | Surface | | |
| Chain length | $D_0$ | $E_a^D$ | $R^2$ | $D_0$ | $E_a^D$ | $R^2$ | $D_0$ | $E_a^D$ | $R^2$ |
|---|---|---|---|---|---|---|---|---|---|
| 10 | 5.551 | 1.977 | 0.936 | 1.881 | 1.607 | 0.989 | 3.713 | 1.705 | 0.925 |
| 20 | 2.869 | 2.116 | 0.984 | 0.314 | 1.222 | 0.962 | 0.868 | 1.327 | 0.959 |
| 30 | 2.801 | 2.213 | 0.995 | 0.261 | 1.215 | 0.956 | 0.257 | 1.029 | 0.837 |
| 40 | 2.165 | 2.301 | 0.976 | 0.345 | 1.301 | 0.971 | 0.364 | 1.172 | 0.964 |

temperature is $\sim 37$ mNm$^{-1}$ and the experimental surface tension values so far 21–36 mNm$^{-1}$ (Refs. 49–51) agree with this prediction.

## B. Chain dynamics

The macroscopic properties of P3HT films are greatly associated with the chain dynamics in the film; therefore, there is great interest in understanding the P3HT chain dynamics. The polymer chain dynamics and relaxations occur in a wide range of time scales, from picoseconds (conformational transition) to nanoseconds (segmental relaxation) and to seconds. The conformational transition can be studied by calculating the backbone torsion autocorrelation time. The segmental relaxation can be determined by looking at the chain self-diffusion and rotational reorientation. Self-diffusion includes both chain center-of-mass diffusion and chain segment diffusion. Rotational relaxation can be determined by calculating the first-order and second-order end-to-end vector autocorrelation times. To describe the dynamics of the chain in different parts of the films, we divide the film into two major regions: "bulk" is the middle part of the film where the mass density is constant, and "surface" is the interfacial side of the film where the mass density is less than 90% of the bulk mass density. For the 10-mers chains, the dynamic quantities at 660 K were calculated long before any chain degradation was observed.

### 1. Self-diffusion coefficient

Chain translational dynamics can be easily analyzed by monitoring the motion of the whole-chain and chain-segment (thiophene ring) center-of-mass as a function of time. The mean square displacement (MSD) of the centers-of-mass is defined as

$$g_{cm}(t) = \left\langle \frac{1}{N_c} \sum_{i=1}^{N_c} [R_{i,cm}(t+t_0) - R_{i,cm}(t_0)]^2 \right\rangle, \quad (9)$$

where angle brackets denote an ensemble average overall time origins $t_0$, and $R_{i,cm}(t)$ is the position of the center-of-mass of the chain or chain segment $i$ at time $t$. The self-diffusion coefficient $D$ of the thiophene ring segment is computed from the slope of the MSD in the linear regime using the Einstein relation,[61]

$$D = \lim_{t \to \infty} \frac{1}{6t} g_{cm}(t). \quad (10)$$

Figure 8 shows the chain center-of-mass diffusion coefficient as a function of temperature. The diffusion coefficient increases with increasing temperature and decreasing chain length. The diffusion coefficient for 10-mers chains is much higher than for other chain lengths. The differences can be attributed to the mass densities in the bulk region; the lower the density, the higher the diffusion coefficients.
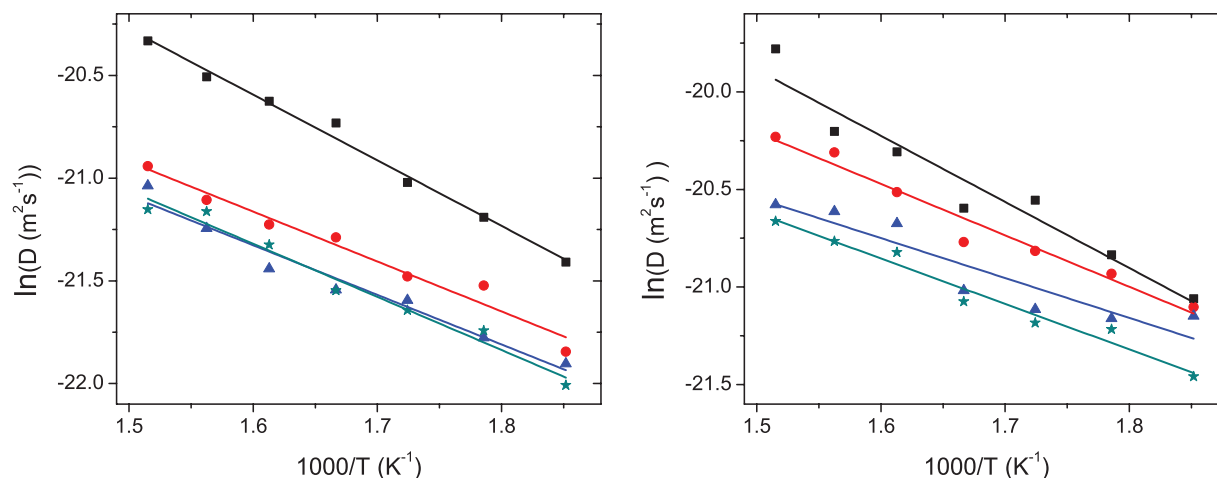


FIG. 9. Thiophene ring diffusion coefficient as a function of temperature for different film region: bulk (left) and surface (right). Depicted systems are composed of chains of length 10 (squares), 20 (circles), 30 (triangles), and 40 (stars) monomers. The solid lines are fits to the data using Eq. (11).
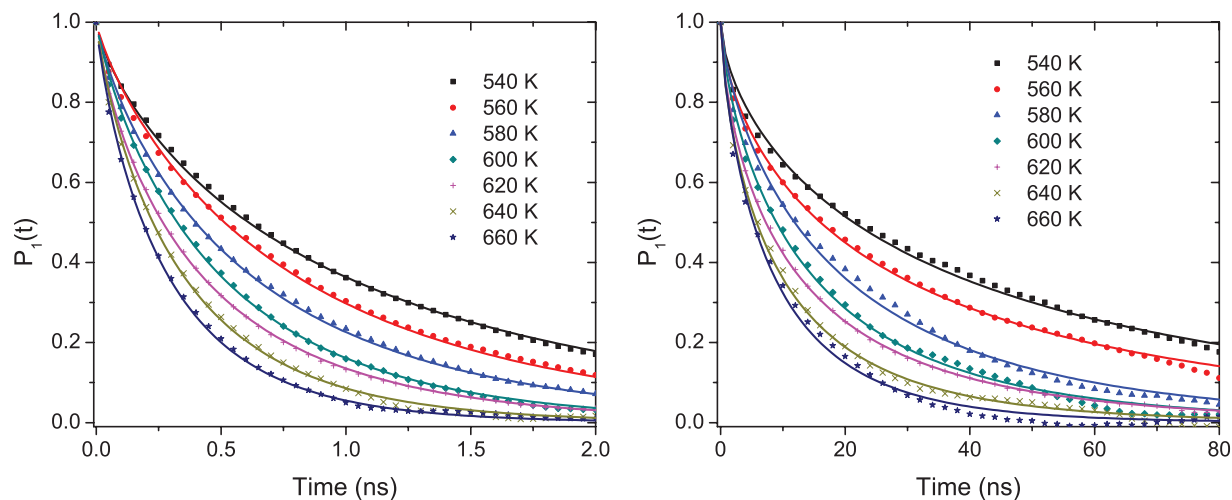
FIG. 10. Time decay of the first-order end-to-end vector orientational autocorrelation function, $P_1(t)$, at seven different temperatures (from 540 K to 660 K in steps of 20 K) for systems of 10-mers chains (left), and 40-mers chains (right). The solid lines are fits to the data using Eq. (14).

The temperature dependence of the diffusion coefficient is usually described using an Arrhenius relation

$$D(T) = D_0 \exp\left(\frac{-E_a^D}{RT}\right), \quad (11)$$

where $E_a^D$ is the apparent activation energy, $R$ is the ideal gas constant, and $D_0$ is the diffusion coefficient at infinite temperature. This fits the chain center-of-mass diffusion coefficient data very well as shown by the solid lines in Figure 8. The parameters extracted from the fitting are tabulated in Table VI. As expected $E_a^D$ increases and $D_0$ decreases as the chain length increases.

For thin films, part of a chain can be in bulk and the other part of the chain in the surface region. Chain segments at the surface have more free volume compared to those in bulk, and the chain dynamics in the two regions are therefore different. For the two film regions, we looked at the MSD of the thiophene ring center-of-mass and two different components of the same chain, namely, the normal component

(along the surface normal) and the lateral component (parallel to the film surface). In the bulk, the time rates of change of the MSD for the normal and lateral components are similar, which implies isotropic chain dynamics. However, at the surface, the time rate of change of the MSD of the lateral component is larger than that of the normal component, which implies anisotropic chain dynamics in this region. To quantify this for both regions, we calculated the diffusion coefficients of the thiophene rings, and the results are tabulated in Table VI.

Figure 9 shows the temperature dependence of the thiophene ring diffusion coefficient in both bulk and surface region. The diffusion coefficient increases with increasing temperature and decreasing chain length. The diffusion coefficient in the surface region is higher than in the bulk and it also shows strong chain-length dependence in the surface region compared to in the bulk. The diffusion coefficient data were fit to Eq. (11) and are shown by the solid lines in Figure 9. The values of $D_0$ and $E_a^D$ obtained from the fits are tabulated
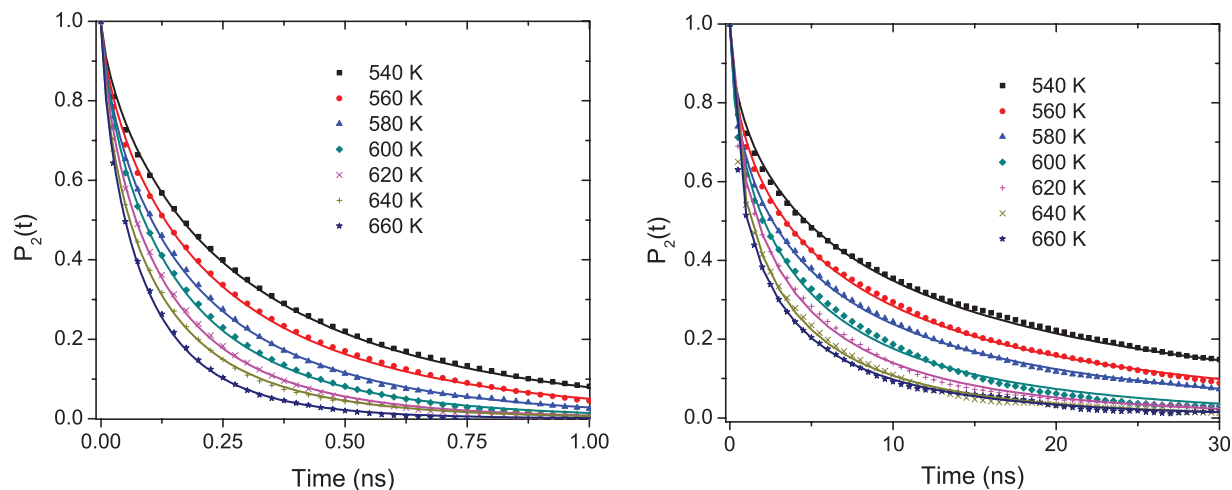


FIG. 11. Time decay of the second-order end-to-end vector orientational autocorrelation function, $P_2(t)$, at seven different temperatures (from 540 K to 660 K in steps of 20 K) for systems of 10-mers chains (left), and 40-mers chains (right). The solid lines are fits to the data using Eq. (14).

TABLE VII. Parameters obtained from fitting first-order and second-order end-to-end vector orientational autocorrelation functions.

| | 10-mers chains | | | | | | | 20-mers chains | | | | | | |
| | $P_1(t)$ | | | $P_2(t)$ | | | | $P_1(t)$ | | | $P_2(t)$ | | | |
| $T(K)$ | $\tau_1$(ns) | $\beta_1$ | $\tau_1^c$(ns) | $\tau_2$(ns) | $\beta_2$ | $\tau_2^c$(ns) | $\tau_1^c/\tau_2^c$ | $\tau_1$(ns) | $\beta_1$ | $\tau_1^c$(ns) | $\tau_2$(ns) | $\beta_2$ | $\tau_2^c$(ns) | $\tau_1^c/\tau_2^c$ |
|---|---|---|---|---|---|---|---|---|---|---|---|---|---|---|
| 540 | 0.984 | 0.767 | 1.151 | 0.275 | 0.722 | 0.339 | 3.394 | 5.785 | 0.771 | 6.739 | 1.574 | 0.625 | 2.251 | 2.993 |
| 560 | 0.795 | 0.839 | 0.872 | 0.218 | 0.719 | 0.269 | 3.239 | 5.072 | 0.723 | 6.231 | 1.293 | 0.629 | 1.832 | 3.401 |
| 580 | 0.619 | 0.828 | 0.685 | 0.172 | 0.723 | 0.212 | 3.235 | 3.555 | 0.791 | 4.060 | 1.006 | 0.618 | 1.459 | 2.784 |
| 600 | 0.497 | 0.860 | 0.536 | 0.144 | 0.744 | 0.173 | 3.108 | 2.881 | 0.771 | 3.355 | 0.781 | 0.645 | 1.076 | 3.118 |
| 620 | 0.421 | 0.800 | 0.477 | 0.118 | 0.735 | 0.144 | 3.322 | 2.211 | 0.770 | 2.579 | 0.601 | 0.637 | 0.841 | 3.066 |
| 640 | 0.348 | 0.851 | 0.378 | 0.099 | 0.699 | 0.126 | 2.994 | 1.879 | 0.753 | 2.231 | 0.510 | 0.658 | 0.688 | 3.243 |
| 660 | 0.286 | 0.851 | 0.311 | 0.082 | 0.739 | 0.098 | 3.166 | 1.441 | 0.765 | 1.689 | 0.407 | 0.655 | 0.552 | 3.059 |
| | 30-mers chains | | | | | | | 40-mers chains | | | | | | |
| | $P_1(t)$ | | | $P_2(t)$ | | | | $P_1(t)$ | | | $P_2(t)$ | | | |
| $T(K)$ | $\tau_1$(ns) | $\beta_1$ | $\tau_1^c$(ns) | $\tau_2$(ns) | $\beta_2$ | $\tau_2^c$(ns) | $\tau_1^c/\tau_2^c$ | $\tau_1$(ns) | $\beta_1$ | $\tau_1^c$(ns) | $\tau_2$(ns) | $\beta_2$ | $\tau_2^c$(ns) | $\tau_1^c/\tau_2^c$ |
| 540 | 14.762 | 0.688 | 19.007 | 3.877 | 0.574 | 6.188 | 3.071 | 37.601 | 0.649 | 51.473 | 9.089 | 0.547 | 15.589 | 3.302 |
| 560 | 12.926 | 0.663 | 17.290 | 3.237 | 0.570 | 5.221 | 3.312 | 28.290 | 0.646 | 38.889 | 6.619 | 0.556 | 11.092 | 3.506 |
| 580 | 9.602 | 0.704 | 12.083 | 2.547 | 0.554 | 4.286 | 2.819 | 19.493 | 0.741 | 23.432 | 5.139 | 0.541 | 8.955 | 2.617 |
| 600 | 7.703 | 0.599 | 11.617 | 1.826 | 0.562 | 3.008 | 3.862 | 14.716 | 0.736 | 17.796 | 3.917 | 0.588 | 6.048 | 2.942 |
| 620 | 5.793 | 0.748 | 6.914 | 1.586 | 0.598 | 2.395 | 2.887 | 12.481 | 0.676 | 16.351 | 3.162 | 0.588 | 4.887 | 3.346 |
| 640 | 5.101 | 0.714 | 6.336 | 1.325 | 0.562 | 2.183 | 2.903 | 9.708 | 0.707 | 12.168 | 2.482 | 0.576 | 3.946 | 3.083 |
| 660 | 4.025 | 0.687 | 5.185 | 1.031 | 0.581 | 1.622 | 3.197 | 8.532 | 0.757 | 10.078 | 2.118 | 0.544 | 3.667 | 2.748 |

in Table VI. As given in the table, in the bulk, the activation energy increases with increasing chain length. However, in the surface region, the activation energy does not show clear chain-length dependence.

### 2. Chain orientational relaxation

The chain rotational diffusion can be described by quantifying the rate of reorientation of a chain end-to-end vector. The reorientation (relaxation) time of a chain is determined by monitoring the decay of the auto-correlation function of the end-to-end vector. The first-order and second-order end-to-end vector autocorrelation functions (OACF) are given by the respective expressions

$$P_1(t) = \left\langle \frac{1}{N_C} \sum_i^{N_C} R_i(t + t_0) \cdot R_i(t_0) \right\rangle, \qquad (12)$$

$$P_2(t) = \frac{1}{2} \left\langle 3 \frac{1}{N_C} \sum_i^{N_C} [R_i(t + t_0) \cdot R_i(t_0)]^2 - 1 \right\rangle, \qquad (13)$$

where angle brackets represent ensemble averages, which range overall time origins $t_0$; $N_C$ is the total number of P3HT chains; and $R_i(t)$ is a unit vector along the end-to-end vector of chain $i$ at time $t$. For two representative chain lengths (10 and 40 monomers), the calculated values of $P_1(t)$ and $P_2(t)$ as functions of time are shown in Figures 10 and 11,
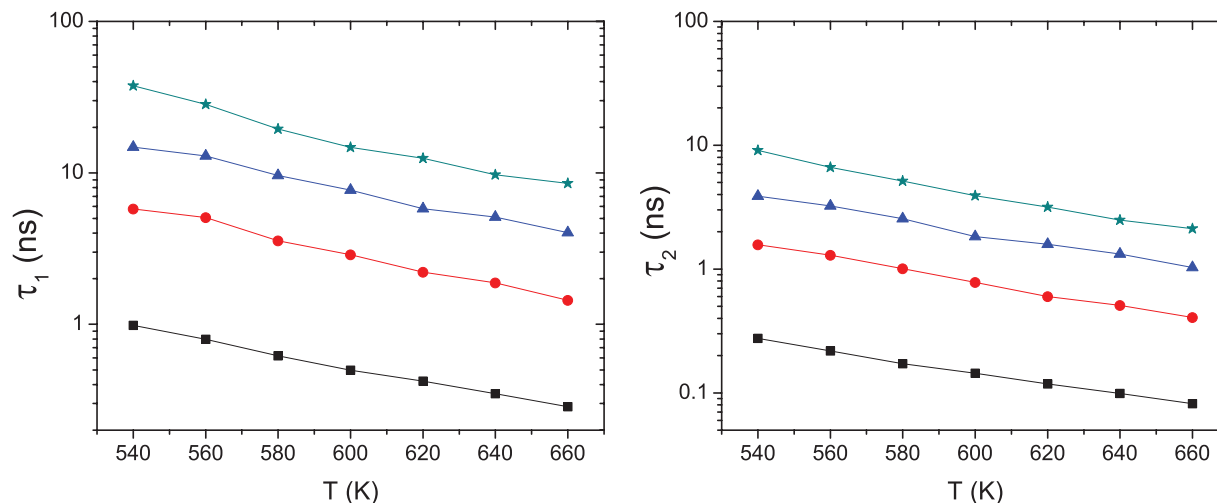


FIG. 12. Relaxation times as a function of temperature: $\tau_1$ (left) and $\tau_2$ (right). Systems are composed of chains of length 10 (squares), 20 (circles), 30 (triangles), and 40 (stars) monomers. The solid lines are guides to the eye.
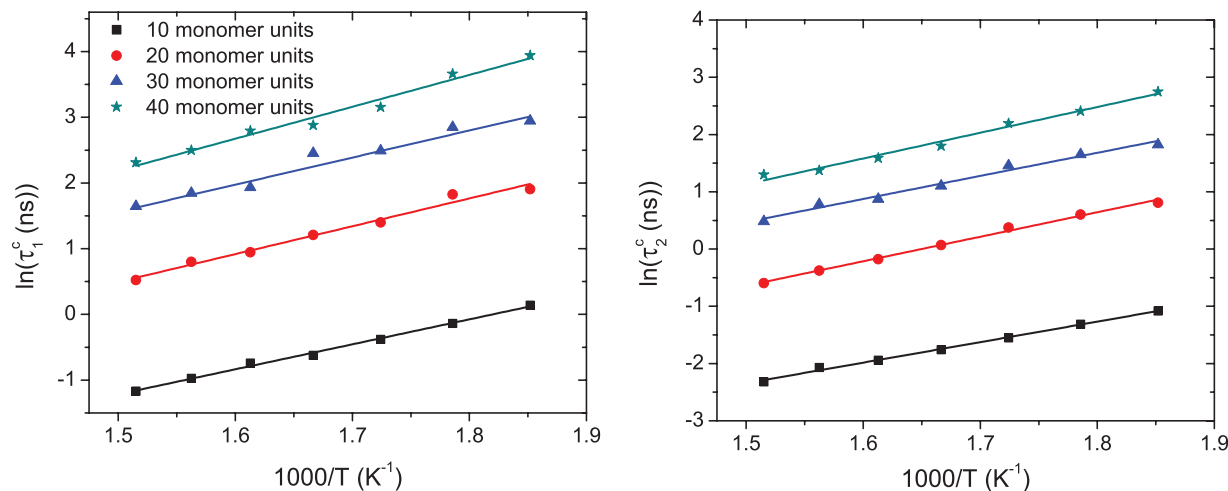
FIG. 13.  Correlation time as a function of temperature for $\tau_1^c$ (left) and $\tau_2^c$ (right). Systems composed of chains of length 10 (squares), 20 (circles), 30 (triangles), and 40 (stars) monomers. The solid lines are the fits to the data using Eq. (16).

respectively. As depicted in the figures, the decay times for both OACFs, $P_1(t)$ and $P_2(t)$, increase with increasing chain length and decreasing temperature.

The OACFs, $P_1(t)$ and $P_2(t)$, were fit to the Kohlrausch-Williams-Watts (KWW) equation[62]

$$P_i^{KWW}(t) = \exp(-(t/\tau_i)^{\beta_i}), \tag{14}$$

where $i = 1$ for first-order and $i = 2$ for second-order, $\tau_i$ is the relaxation time, and $\beta_i$ ($0 < = \beta_i < = 1$) is a measure of the width of the distribution of the specific relaxation processes expressed by $P_i(t)$. The parameter $\beta_i$ is equal to unity for a single exponential and decreases as the width of the distribution becomes broader. In Figures 10 and 11, Eq. (14) is shown to fit the $P_1(t)$ and $P_2(t)$ data very well. The parameters $\tau_i$ and $\beta_i$ obtained from the fitting are tabulated in Table VII. As shown in the table, all the values of $\beta_i$ are less than unity, implying there are multiple relaxation modes. Moreover, the values of $\beta_i$ for shorter chain lengths and higher temperatures are larger than for longer chain lengths and lower temperatures.

The relaxation times $\tau_1$ and $\tau_2$ are plotted as functions of temperature for four different chain lengths in Figure 12. Both $\tau_1$ and $\tau_2$ increase with increasing chain length and decreasing temperature. For longer chain lengths or shorter chains at lower temperatures, the chain dynamics become slow, which leads to long relaxation times. This explains why equilibration of the liquid/vacuum interface to calculate reliable surface tension data required very long simulation time for the longer-chain films or shorter chains at lower temperatures.

More quantitatively, to characterize the cooperative chain dynamics, the correlation times $\tau_i^c$ ($\tau_1^c$ and $\tau_2^c$) were calculated using

$$\tau_i^c = \int_0^\infty \exp(-(t/\tau_i)^{\beta_i})dt = \tau_i \frac{\Gamma(1/\beta_i)}{\beta_i}, \tag{15}$$

where $\Gamma$ is the gamma function. Using Eq. (15), the calculated correlation times $\tau_1^c$ and $\tau_2^c$ for different systems are tabulated in Table VII. The ratio of $\tau_1^c/\tau_2^c$, as shown in the table, is different from three implying the rotational diffusion of the chains are anisotropic.[63] The temperature dependence of $\tau_1^c$ and $\tau_2^c$ is shown in Figure 13. The correlation time, as can be seen in the figure, increases with increasing chain length and decreasing temperature. In the figure, the observed linear dependence of $ln(\tau_i^c)$ versus $1/T$ for the correlation time indicates that this process includes thermally activated motions described by the Arrhenius equation

$$\tau_i^c = \tau_{0,i}^c \exp\left(\frac{E_{a,i}^c}{RT}\right), \tag{16}$$

where $E_{a,i}^c$ is the apparent activation energy and $\tau_{0,i}^c$ is the pre-exponential factor. In Figure 13, shown by the solid lines, Eq. (16) fits the correlation time data very well. The parameters $E_{a,i}^c$ and $\tau_{0,i}^c$ obtained from the fitting are tabulated in Table VIII. The apparent activation energy for both correlation times increases with increasing chain length.

TABLE VIII.  Values of parameters obtained from fitting $\tau_1^c$ and $\tau_2^c$ data using Eq. (16).

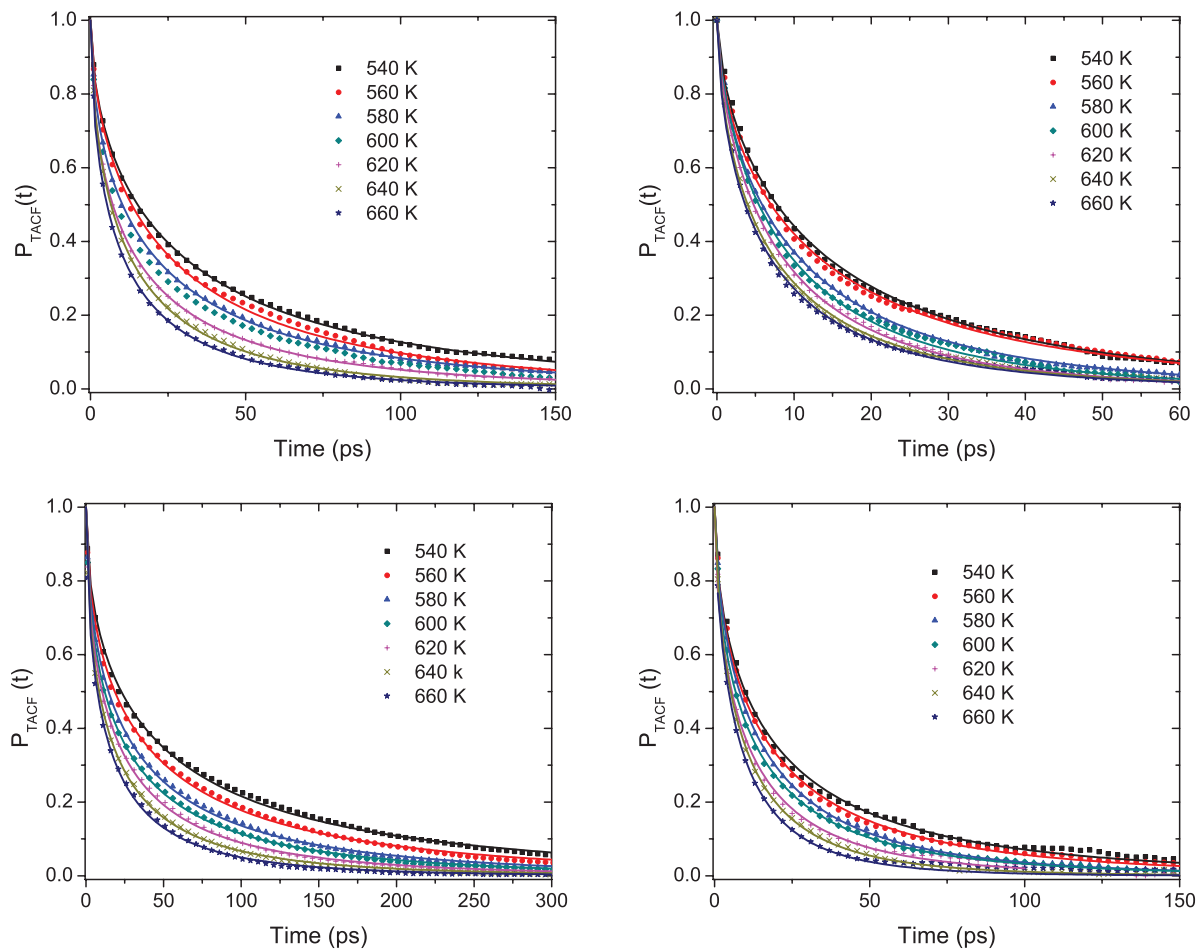| Chain length | $\tau_1^c$ | | | $\tau_2^c$ | | |
|---|---|---|---|---|---|---|
| | $\tau_{0,1}^c (\times 10^{-3}$ ns$)$ | $E_{a,1}^c$(kcal mol$^{-1}$) | $R^2$ | $\tau_{0,2}^c (\times 10^{-3}$ ns$)$ | $E_{a,2}^c$(kcal mol$^{-1}$) | $R^2$ |
| 10 | 0.991 | 1.913 | 0.996 | 0.447 | 1.802 | 0.996 |
| 20 | 2.840 | 2.133 | 0.980 | 0.859 | 2.153 | 0.994 |
| 30 | 9.850 | 2.074 | 0.978 | 3.787 | 2.029 | 0.982 |
| 40 | 6.116 | 2.444 | 0.975 | 3.663 | 2.262 | 0.983 |

FIG. 14. Time decay of the torsion autocorrelation function, $P_{TACF}(t)$, for 10-mers chains (top raw) and 40-mers chains (bottom raw) at seven different temperatures (from 540 K to 660 K in steps of 20 K) in bulk (left column), and surface region (right column). The solid lines are fits to the data using Eq. (14).

TABLE IX. Parameters extracted from fitting the torsion autocorrelation time using Eq. (14).

| | 10-mers chains | | | | | | 20-mers chains | | | | | |
|---|---|---|---|---|---|---|---|---|---|---|---|---|
| | Bulk | | | Surface | | | Bulk | | | Surface | | |
| T (K) | $\tau_3$(ps) | $\beta_3$ | $\tau_3^c$(ps) | $\tau_3$(ps) | $\beta_3$ | $\tau_3^c$(ps) | $\tau_3$(ps) | $\beta_3$ | $\tau_3^c$(ps) | $\tau_3$(ps) | $\beta_3$ | $\tau_3^c$(ps) |
| 540 | 28.570 | 0.578 | 45.260 | 13.660 | 0.648 | 18.739 | 42.755 | 0.534 | 76.205 | 19.385 | 0.585 | 30.188 |
| 560 | 24.459 | 0.601 | 36.727 | 12.586 | 0.626 | 17.942 | 31.249 | 0.551 | 53.016 | 16.997 | 0.549 | 27.097 |
| 580 | 19.768 | 0.561 | 32.646 | 10.157 | 0.664 | 13.552 | 25.494 | 0.551 | 43.308 | 12.425 | 0.598 | 18.941 |
| 600 | 17.251 | 0.557 | 28.912 | 9.249 | 0.687 | 11.931 | 21.278 | 0.542 | 37.038 | 10.528 | 0.605 | 15.683 |
| 620 | 13.899 | 0.550 | 23.648 | 8.165 | 0.677 | 10.681 | 17.716 | 0.548 | 30.357 | 10.620 | 0.601 | 15.954 |
| 640 | 12.215 | 0.588 | 18.879 | 7.075 | 0.637 | 9.888 | 14.565 | 0.563 | 23.954 | 8.623 | 0.617 | 12.519 |
| 660 | 10.036 | 0.573 | 16.086 | 6.563 | 0.628 | 9.332 | 12.567 | 0.563 | 20.663 | 7.814 | 0.613 | 11.440 |
| | 30-mers chains | | | | | | 40-mers chains | | | | | |
| | Bulk | | | Surface | | | Bulk | | | Surface | | |
| T (K) | $\tau_3$(ps) | $\beta_3$ | $\tau_3^c$(ps) | $\tau_3$(ps) | $\beta_3$ | $\tau_3^c$(ps) | $\tau_3$(ps) | $\beta_3$ | $\tau_3^c$(ps) | $\tau_3$(ps) | $\beta_3$ | $\tau_3^c$(ps) |
| 540 | 42.126 | 0.538 | 77.106 | 18.842 | 0.581 | 29.619 | 45.041 | 0.535 | 80.052 | 18.583 | 0.578 | 29.433 |
| 560 | 34.397 | 0.547 | 59.033 | 15.738 | 0.564 | 25.830 | 36.404 | 0.541 | 63.586 | 16.656 | 0.587 | 25.806 |
| 580 | 28.036 | 0.549 | 47.869 | 15.051 | 0.572 | 24.173 | 28.320 | 0.547 | 48.585 | 14.485 | 0.622 | 20.844 |
| 600 | 23.136 | 0.527 | 42.127 | 11.994 | 0.578 | 18.963 | 23.664 | 0.538 | 41.682 | 12.488 | 0.591 | 19.147 |
| 620 | 18.625 | 0.547 | 31.952 | 9.859 | 0.604 | 14.706 | 20.112 | 0.549 | 34.380 | 10.216 | 0.596 | 15.506 |
| 640 | 15.753 | 0.552 | 26.686 | 8.508 | 0.602 | 12.652 | 16.357 | 0.549 | 27.941 | 9.227 | 0.631 | 13.044 |
| 660 | 13.420 | 0.552 | 22.689 | 7.891 | 0.621 | 11.375 | 13.982 | 0.558 | 23.296 | 7.978 | 0.645 | 10.993 |
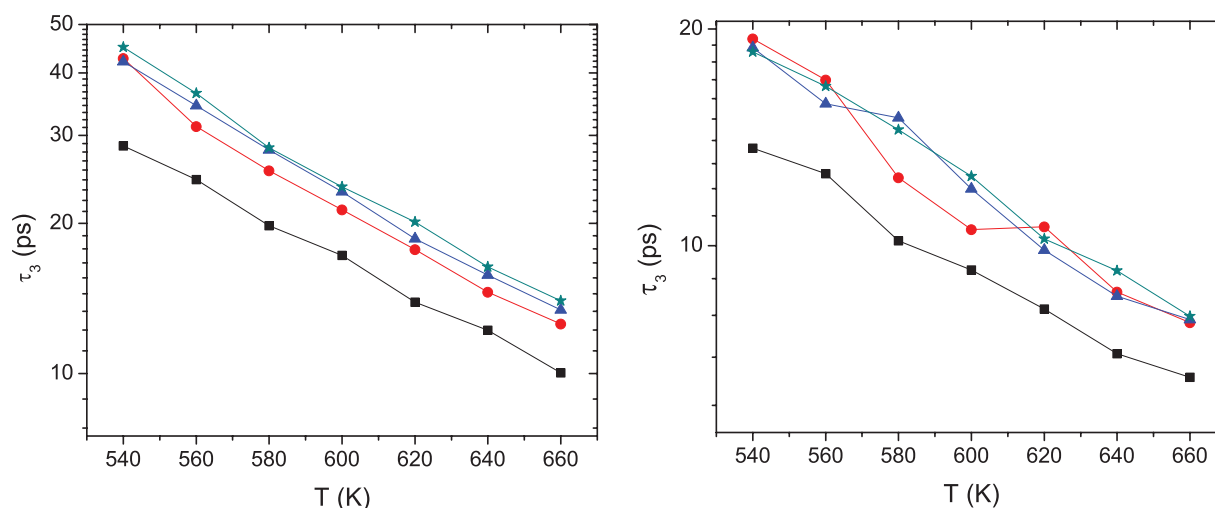
FIG. 15. Chain torsion relaxation time as a function of temperature in bulk (left) and surface region (right). Systems composed of chains of length 10 (squares), 20 (circles), 30 (triangles), and 40 (stars) monomers. The solid lines are guides to the eye.

### 3. Torsional autocorrelation

Polymer dynamics can be determined by calculating conformational dynamics and relaxation. Conformational dynamics can be related to the torsional transition, whereas torsional relaxation can be described by the torsion autocorrelation function (TACF). Experimentally, the TACF can be quantified using dielectric relaxation, T1 spin-lattice relaxation and viscosity measurements. The conformations of the chain backbones were investigated by looking at the TACF, defined by

$$P_{TACF}(t) = \frac{\langle \cos\phi(t+t_0)\cos\phi(t_0)\rangle - \langle\cos\phi(t_0)\rangle^2}{\langle\cos\phi(t_0)\cos\phi(t_0)\rangle - \langle\cos\phi(t_0)\rangle^2}, \quad (17)$$

where $\phi(t)$ is the backbone chain torsion angle at time $t$. For different systems, the TACF for the bulk and in the surface region of the films were calculated using Eq. (17). Figure 14 shows the time decay of the TACF for 10- and 40-mers chains in bulk and in the surface region at different temperatures.

The TACF was also fit to the stretched exponential given in Eq. (14) (with $i = 3$), and from this, we derive $\tau_3$ and

$\beta_3$ for the relaxation times and widths of the distributions, respectively. In Figure 14, shown by the solid lines, TACFs fit the data well using Eq. (14). The parameters $\tau_3$ and $\beta_3$ obtained from the fitting are shown in Table IX, along with correlation times ($\tau_3^c$) calculated using Eq. (15) (with $i = 3$). $\beta_3$ decreases with increasing chain length, implying that the longer the chain, the lower the cooperativeness of the chain conformational reorientation. Moreover, $\beta_3$ values in the surface region are smaller than those in bulk.

The torsional relaxation time, $\tau_3$, is plotted as a function of temperature in Figure 15. As shown in the figure, the torsion relaxation time in bulk is much larger than in the surface region because there is large free-volume in the surface region which allows the torsion to relax faster. The chain-length dependence of the torsion relaxation time follows the same trend as the mass density because the torsion relaxation time is also related to the chain packing: the denser the chain packing, the longer the relaxation time.

In Figure 16, the torsion correlation time $\tau_3^c$ is shown as a function of temperature. As depicted in the figure, $ln(\tau_3^c)$
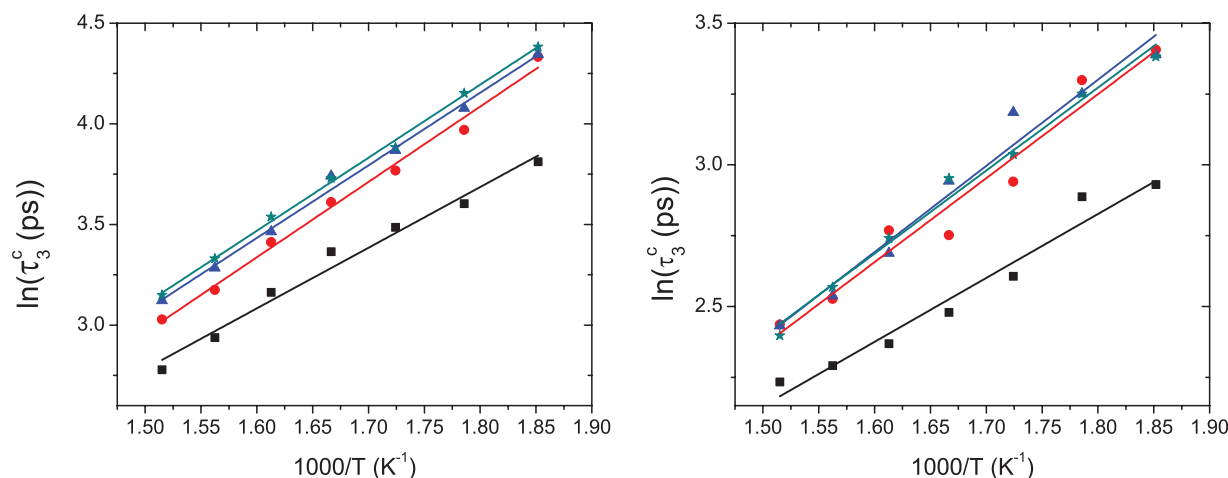


FIG. 16. Chain torsion correlation time as a function of temperature for bulk (left) and surface (right). Systems composed of chains of length: 10 (squares), 20 (circles), 30 (triangles), and 40 (stars) monomers. The solid lines are fits to the data using Eq. (16).

TABLE X. Parameters extracted from fitting the torsion correlation time using Eq. (16).

| Chain length | Bulk | | | Surface | | |
|---|---|---|---|---|---|---|
| | $\tau_{0,3}^c(\times 10^{-3}\text{ps})$ | $E_{a,3}^c(\text{kcal mol}^{-1})$ | $R^2$ | $\tau_{0,3}^c(\times 10^{-3}\text{ps})$ | $E_{a,3}^c(\text{kcal mol}^{-1})$ | $R^2$ |
| 10 | 0.175 | 1.517 | 0.978 | 0.290 | 1.137 | 0.956 |
| 20 | 0.071 | 1.884 | 0.991 | 0.124 | 1.492 | 0.951 |
| 30 | 0.096 | 1.815 | 0.994 | 0.114 | 1.530 | 0.966 |
| 40 | 0.096 | 1.827 | 0.996 | 0.136 | 1.474 | 0.985 |

vs $1/T$ shows linear dependence, which indicates that the process is thermally activated. The torsion correlation times fit Eq. (16) very well, as shown by the solid lines in Figure 16. The activation energy $E_{a,3}^c$ and the pre-exponential factor $\tau_{0,3}^c$ obtained from the fitting are tabulated in Table X. As shown in the table, the activation energy increases with increasing chain length. Moreover, the activation energy is larger in the bulk than in the surface region.

## IV. SUMMARY AND CONCLUSIONS

In this study, using all-atom molecular dynamics simulations, we investigated the dependence of both static and dynamic properties of P3HT at liquid/vacuum interfaces on molecular weight (chain length) and temperature. To characterize the static properties of the films, we calculated specific volume, interfacial width, orientational ordering of the hexyl groups and surface tension. The molecular weight dependence of specific volume was significant, and was found to obey the Simha-Somcynsky's equation of state. The interfacial width, in general, showed an increasing trend with increasing temperature but with no clear dependence on molecular weight at low temperatures. However, the orientational ordering calculations showed the hexyl groups protruding from the vacuum side of the interface where the degree of order at the interface was found to be strongly dependent on both temperature and molecular weight. This resulted the surface tension to be strongly dependent on molecular weight and temperature. The surface tension values showed a linear dependence on temperature and the molecular weight dependence was equally described by both $M^{-2/3}$ and $M^{-1}$ power law models.

The dynamic properties were quantified by calculating diffusion coefficients for the chain centers-of-mass and thiophene ring segments, as well as first-order and second-order end-to-end vector autocorrelation times, and the chain backbone torsion autocorrelation time. The chain center-of-mass and thiophene ring segment diffusion coefficient showed strong molecular weight dependence. The temperature dependence of both diffusion coefficients followed an Arrhenius relation. The diffusion coefficient of the thiophene ring segment in the surface region was higher than in the bulk. Moreover, the chain segment diffusion at the surface was anisotropic, whereas in the bulk it was isotropic. The first-order and second-order end-to-end vector autocorrelations and the torsion autocorrelation were well described by KWW equation. The chain rotational relaxation and torsion relaxation showed

strong molecular weight dependence. The temperature dependence of both relaxation times also exhibited the Arrhenius behavior. The torsion relaxation time of the backbone of a chain was found to be smaller in the surface region than in the bulk.

In conclusion, our simulation results should be very helpful in elucidating the interfacial properties of P3HT based solar cells at the molecular level. The quantities we obtained from static and dynamic calculations are important in characterizing the structure and morphology of P3HT at the interfaces. For example, the surface tension can be very helpful in choosing a substrate to produce a head-on or face-on orientation of P3HT chain, which plays crucial role in determining the charge collection at electrodes (interfaces), or in predicting whether the P3HT can mix with another polymer. In general, detailed analysis of the static and dynamic properties of P3HT films show that the calculated static and dynamic properties data can be fit with well-known polymer models.

[1] A. O. Patil, A. J. Heeger, and F. Wudl, Chem. Rev. **88**, 183 (1988).
[2] W. Y. Huang, C. C. Lee, S. G. Wang, Y. K. Han, and M. Y. Chang, J. Electrochem. Soc. **157**, B1336 (2010).
[3] Z. Bao, A. Dodabalapur, and A. J. Lovinger, Appl. Phys. Lett. **69**, 4108 (1996).
[4] S.-H. Lee, J.-H. Kim, T.-H. Shim, and J.-G. Park, Electron. Mater. Lett. **5**, 47 (2009).
[5] S.-H. Lee, D.-H. Kim, J.-H. Kim, G.-S. Lee, and J.-G. Park, J. Phys. Chem. C **113**, 21915 (2009).
[6] M. C. Scharber, D. Mühlbacher, M. Koppe, P. Denk, C. Waldauf, A. J. Heeger, and C. J. Brabec, Adv. Mater. **18**, 789 (2006).
[7] C. H. Peters, I. T. Sachs-Quintana, J. P. Kastrop, S. Beaupré, M. Leclerc, and M. D. McGehee, Adv. Energy Mater. **1**, 491 (2011).
[8] N. D. Treat, M. A. Brady, G. Smith, M. F. Toney, E. J. Kramer, C. J. Hawker, and M. L. Chabinyc, Adv. Energy Mater. **1**, 82 (2011).
[9] D. Chen, F. Liu, C. Wang, A. Nakahara, and T. P. Russell, Nano Lett. **11**, 2071 (2011).
[10] S. S. v. Bavel, E. Sourty, G. d. With, and J. Loos, Nano Lett. **9**, 507 (2009).
[11] K. Vakhshouri, D. R. Kozub, C. Wang, A. Salleo, and E. D. Gomez, Phys. Rev. Lett. **108**, 026601 (2012).
[12] D. H. Kim, Y. Jang, D. Y. Park, and K. Cho, Macromolecules **39**, 5843 (2006).
[13] M. C. Gurau, D. M. Delongchamp, B. M. Vogel, E. K. Lin, D. A. Fischer, S. Sambasivan, and L. J. Richter, Langmuir **23**, 834 (2007).
[14] Y. Y. Yimer, A. Dhinojwala, and M. Tsige, J. Chem. Phys. **137**, 044703 (2012).

[15] M.-C. Wu, C.-H. Chang, H.-H. Lo, Y.-S. Lin, Y.-Y. Lin, W.-C. Yen, W.-F. Su, Y.-F. Chen, and C.-W. Chen, J. Mater. Chem. **18**, 4097 (2008).

[16] C. Goh, R. J. Kline, M. D. McGehee, E. N. Kadnikova, and J. M. J. Fréchet, Appl. Phys. Lett. **86**, 122110 (2005).

[17] A. J. Moulé and K. Meerholz, Adv. Mater. **20**, 240 (2008).

[18] D. M. Huang, R. Faller, K. Do, and A. J. Moulè, J. Chem. Theory Comput. **6**, 526 (2010).

[19] K. Do, D. M. Huang, R. Faller, and A. J. Moulé, Phys. Chem. Chem. Phys. **12**, 14735 (2010).

[20] D. M. Huang, A. J. Moulè, and R. Faller, Fluid Phase Equilib. **302**, 21 (2011).

[21] V. Marcon and G. Raos, J. Am. Chem. Soc. **128**, 1408 (2006).

[22] S. B. Darling and M. Sternberg, J. Phys. Chem. B **113**, 6215 (2009).

[23] W. L. Jorgensen, D. S. Maxwell, and J. Tirado-Rives, J. Am. Chem. Soc. **118**, 11225 (1996).

[24] Z. Wu, A. Petzold, T. Henze, T. Thurn-Albrecht, R. H. Lohwasse, M. Sommer, and M. Thelakkat, Macromolecules **43**, 4646 (2010).

[25] C. Muller, T. A. M. Ferenczi, M. Campoy-Quiles, J. M. Frost, D. D. C. Bradley, P. Smith, N. Stingelin-Stutzmann, and J. Nelson, Adv. Mater. **20**, 3510 (2008).

[26] T. A. Chen, X. Wu, and R. D. Rieke, J. Am. Chem. Soc. **117**, 233 (1995).

[27] D. E. Motaung, G. F. Malgas, C. J. Arendse, S. E. Mavundla, C. J. Oliphant, and D. Knoesen, Sol. Energy Mater. Sol. Cells **93**, 1674 (2009).

[28] R. Qian, S. Chen, W. Song, and X. Bi, Macromol. Rapid Commun. **15**, 1 (1994).

[29] S. Plimpton, J. Comput. Phys. **117**, 1 (1995).

[30] R. Hockney and J. Eastwood, *Computer Simulation Using Particles* (Hilger, New York, 1988).

[31] F. A. Escobedo and Z. Chen, J. Chem. Phys. **121**, 11463 (2004).

[32] M. A. Amat and G. C. Rutledge, J. Chem. Phys. **132**, 114704 (2010).

[33] D. N. Theodorou, Macromolecules **22**, 4578 (1989).

[34] Y. B. Tatek and M. Tsige, J. Chem. Phys. **135**, 174708 (2011).

[35] A. E. Ismail, G. S. Grest, and M. J. Stevens, J. Chem. Phys. **125**, 014702 (2006).

[36] M. D. Lacasse, G. S. Grest, and A. J. Levine, Phys. Rev. Lett. **80**, 309 (1998).

[37] F. Ouhib, R. C. Hiorns, R. de Bettignies, S. Bailly, J. Desbrieres, and C. Dagron-Lartigau, Thin Solid Films **516**, 7199 (2008).

[38] P. Zoller, J. Polym. Sci, Polym. Phys. Ed. **20**, 1453 (1982).

[39] R. Simha and T. Somcynsky, Macromolecules **2**, 342 (1969).

[40] T. G. Fox and P. J. Flory, J. Polym. Sci. **14**, 315 (1954).

[41] T. G. Fox and S. Loshaek, J. Polym. Sci. **15**, 371 (1955).

[42] T. G. Fox and P. J. Flory, J. Appl. Phys. **21**, 581 (1954).

[43] K. Ueberreiter and G. Kanig, Z. Naturforsch. A **6**, 551 (1951).

[44] R. Boyer, Rubber Chem. Technol. **36**, 1303 (1963).

[45] J. R. Martin, J. F. Johnson, and A. R. Cooper, J. Macromol. Sci. Rev. Macromol. Chem. **C8**(1), 57 (1972).

[46] G. T. Dee, T. Ougizawa, and D. J. Walsh, Polymer **33**, 3462 (1991).

[47] G. C. East, D. Margerisoann, and E. Pulat, Trans. Faraday Soc. **62**, 1301 (1966).

[48] J. G. Kirkwood and F. P. Buff, J. Chem. Phys. **17**, 338 (1949).

[49] J. Jaczewska, I. Raptis, A. Budkowski, D. Goustouridis, J. Raczkowska, M. Sanopoulou, E. Pamula, A. Bernasik, and J. Rysz, Synth. Met. **157**, 726 (2007).

[50] G. L. Destri, T. F. Keller, M. Catellani, F. Punzo, K. D. Jandt, and G. Marletta, Macromol. Chem. Phys. **212**, 905 (2011).

[51] H. Kim, B. Yoon, J. Sung, D. G. Choi, and C. Park, J. Mater. Chem. **18**, 3489 (2008).

[52] J. J. Jasper, E. R. Kerr, and F. Egorich, J. Am. Chem. Soc. **75**, 5252 (1953).

[53] J. J. Jasper and E. V. Kring, J. Phys. Chem. **59**, 1019 (1955).

[54] G. W. Bender and J. G. L. Gaines, Macromolecules **3**, 128 (1970).

[55] J. G. L. Gaines, Polym. Eng. Sci. **12**, 1 (1972).

[56] S. Prasad, Z. Jiang, S. K. Sinha, and A. Dhinojwala, Phys. Rev. Lett. **101**, 065505 (2008).

[57] S. Wu, *Polymer Interface and Adhesion* (Marcel Dekker, New York, 1982).

[58] B. B. Sauer and G. T. Dee, Macromolecules **27**, 6112 (1994).

[59] Y. Zhao, G. Yuan, and P. Roche, Polymer **36**, 2211 (1995).

[60] J. Zhao, A. Swinnen, G. v. Assche, J. Manca, D. Vanderzande, and B. v. Mele, J. Phys. Chem. B **113**, 1587 (2009).

[61] J. M. Haile, *Molecular Dynamics Simulation: Elementary Methods* (Wiley, New York, 1992).

[62] G. Williams and D. C. Watts, Trans. Faraday Soc. **66**, 80 (1970).

[63] G. D. Smith and D. Y. Yoon, J. Chem. Phys. **100**, 649 (1994).